Journal of The Electrochemical Society

The Electrochemical Society
Advancing solid state & electrochemical science & technology

Low-Temperature Water Electrolysis Under a Sustained pH-Gradient for Electrochemically-Induced Decarbonation of Limestone into Hydrated Lime

To cite this article before publication: Rémy Rouxhet *et al* 2024 *J. Electrochem. Soc.* in press https://doi.org/10.1149/1945-7111/ad73a6

Low-Temperature Water Electrolysis Under a Sustained pH-Gradient for Electrochemically-Induced Decarbonation of Limestone into Hydrated Lime

Journal:	*Journal of The Electrochemical Society*
Manuscript ID	JES-112245.R1
Manuscript Type:	Research Paper
Date Submitted by the Author:	26-Jul-2024
Complete List of Authors:	Rouxhet, Rémy; Université catholique de Louvain Loudeche, Maxime; Université catholique de Louvain Santoro, Ronny; Université catholique de Louvain Proost, Joris; Université catholique de Louvain, Materials and Process Engineering
Keywords:	electrolysis, hydrogen, electrification, limestone, lime

Low-Temperature Water Electrolysis Under a Sustained pH-Gradient for Electrochemically-Induced Decarbonation of Limestone into Hydrated Lime

Rémy Rouxhet, Maxime Loudeche, Ronny Santoro, and Joris Proost[z]

Division of Materials and Process Engineering (IMAP), Université Catholique de Louvain, Louvain-la-Neuve, Belgium

Lime holds considerable potential in diverse environmental applications. However, its current production remains highly carbon-intensive, emitting more than one ton of CO_2 per ton of lime. To address this issue, recent studies have explored the concept of electrifying the decarbonation of limestone to produce hydrated lime. In this work, a two-compartment electrolysis cell capable of producing $Ca(OH)_2$ has been tested at different currents. Precise pH and Ca^{2+} concentration measurements demonstrate that the electrolysis setup is able to dissolve $CaCO_3$ and precipitate $Ca(OH)_2$ with near-perfect efficiencies. Notably, it highlights that Faraday's law and the concept of transport number can be applied to predict both the equilibrium and kinetic behavior of each step of the process in each of the two cell compartments. Moreover, the use of controlled batch additions of $CaCO_3$ in the system, as opposed to one-time excess addition, was assessed to mitigate the fouling of the cationic exchange membrane used to separate the compartments. Finally, based on the experimental findings, key guidelines are proposed to achieve a perfect reaction stoichiometry for each step. These findings pave the way for a more sustainable and environmentally friendly approach to lime production.

Introduction

Owing to its abundance and alkaline nature, lime is an essential chemical in today's world. In 2019, Europe produced 18.2 million tons of lime [1] which were used in many different areas. Its main application remains in the steel sector, notably for the removal of impurities and as a fluxing agent to reduce the melting temperature of the SiO_2-based slag. More recently, lime has also become a very cost-effective agent in environmental applications to treat flue gases, wastewater, sludges and hazardous wastes. In construction, it is used as a binding agent, as an additive in asphalt and serves soil stabilization purposes. Lime is also vital in various industrial applications such as pulp and paper manufacturing, sugar refining and other chemical uses [2-5].

Lime exists in two forms: quicklime which is calcium oxide (CaO) and slaked lime ($Ca(OH)_2$), also called hydrated lime. The quicklime production process is currently based on the thermal calcination of limestone ($CaCO_3$). This endothermic reaction takes place in a kiln at a temperature between 900 and 1200°C [2, 3] and emits a large amount of process CO_2 process. An additional exothermic hydration step is required to obtain slaked lime.

$$CaCO_{3(s)} + \text{Heat} \rightleftharpoons CaO + CO_2 \quad (1)$$

$$CaO + H_2O \rightleftharpoons Ca(OH)_2 + Heat \quad (2)$$

The current thermal pathway emits more than 1t of CO_2 per ton of lime produced [6, 7], of which around one-third comes from the fuel combustion to reach the kiln temperature. The other two-thirds are process emissions directly linked to the calcination reaction. The increasing European carbon constraints for 2050 drive the lime industry towards a more sustainable production [1]. Current projects to cut lime's carbon footprint include carbon capture from plant flue gas, fossil fuel switching and a more energy-efficient reactor design [8]. Carbon Capture & Storage (CCS) is assumed to have the highest decarbonization potential [9-11]. However, the flue gases of the conventional process are usually quite dilute (~20vol.% of CO_2 [6]) which makes CCS hardly economically viable [12, 13]. Alternative ways to get rid of the calcination reaction gained attention in recent years. Calcination-free production routes offer the opportunity to drastically shift the industry towards a more sustainable process, but still present low technology readiness levels [14, 15].

Among these, a new electrochemical pathway for hydrated lime production has been presented by Ellis *et al.* in 2019 [16]. This innovative route has the major advantage of electrifying the

process, with a decarbonization potential depending on the electricity source. It also produces valuable gases: a pure hydrogen flux and a mixed flow of oxygen and carbon dioxide. The CO_2 content is much higher (66vol.%) compared to the conventional process (~20vol.%), which eases its separation for further sequestration or utilization [12]. This electrochemical pathway is carried out in a so-called hybrid electrolyzer, capable of working with solid, liquid and gaseous phases. The electrolyzer induces $CaCO_3$ dissolution and $Ca(OH)_2$ precipitation at its anodic and cathodic side, respectively, through the exploitation of a pH gradient naturally generated in a neutral water electrolysis cell. All steps occurring to electrochemically convert limestone into hydrated lime are illustrated in Figure 1 and described in more detail below.

The hybrid electrolyzer has several possible configurations [17, 18]. The one selected here is a 2-compartment electrolysis cell composed of an anodic and a cathodic chamber, separated by a cation exchange membrane (CEM). Two electrochemical reactions take place: the oxygen evolution reaction (OER) at the anode and the hydrogen evolution reaction (HER) at the cathode. These half-cell reactions produce protons (H^+) and hydroxide ions (OH^-), respectively, creating a pH gradient within the electrolyzer.

$$\text{Anode (OER): } 2H_2O \rightarrow O_{2(g)} + 4H^+ + 4e^- \quad (3)$$

$$\text{Cathode (HER): } 2H_2O + 2e^- \rightarrow H_{2(g)} + 2OH^- \quad (4)$$

Limestone is added to the anodic chamber where it gets dissolved by the electrochemically generated protons :

$$CaCO_{3(s)} + 2H^+ \rightleftharpoons Ca^{2+} + H_2O + CO_2 \quad (5)$$

Thanks to the effect of the electric field, the dissolved calcium ions then migrate towards the cathodic chamber through the CEM, where they react with the OH^- ions to form the desired final product, calcium hydroxide. The global reaction can be expressed as:

$$2CaCO_{3(s)} + 4H_2O \rightleftharpoons 2Ca(OH)_{2(s)} + 2H_2 + O_2 + 2CO_2 \quad (6)$$

Thanks to the intrinsic potential of this technology, this new field of research has recently gained significant interest. For instance, Conquan *et al.* [17] and Qixian *et al.* [19] confirmed the feasibility of this new electrochemical route. In addition to the production of hydrated lime,

they proposed a reactor allowing the capture of CO_2 from the air with the help of this lime [17] and the electrochemical conversion of the CO_2 produced into valuable hydrocarbon products [19]. More recently, a new type of electrochemical reactor was developed in which CO_2 and O_2 can be recovered separately with a promising low cell voltage [18, 20]. More generally, the idea of exploiting the inherent pH gradient during neutral water electrolysis has also inspired the design of an electrochemical reactor capable of recycling spent cathodes of Li-ion batteries [21].

In this article, we aim at further advancing the operational understanding of the hybrid electrolyzer using a two-compartment cell. Different currents are applied in order to be able to study the intrinsic efficiency of each reaction step. Precise measurements of pH, calcium ion concentration and evolved gas volumes enable the determination and validation of the fundamental laws governing neutral water electrolysis, $CaCO_3$ dissolution, Ca^{2+} migration and $Ca(OH)_2$ precipitation. More precisely, the establishment of a pH gradient and the Ca^{2+} migration efficiency are assessed based on the H^+ and Ca^{2+} transport numbers. The article also investigates the precipitation behavior in the cathodic compartment and its impact on cathodic pH and membrane fouling. To reduce membrane fouling and consider a continuous operation of the reactor, regular additions of $CaCO_3$ are compared with the initial batch addition of $CaCO_3$ in excess. Finally, the article also establishes the process conditions needed for maintaining the stoichiometry of the overall reaction, providing valuable guidelines towards achieving an optimal overall performance.

Experimental

The glass H-cell (Equilabrium) used to carry out all experiments, presented in Figure 2, is filled with 1L of electrolyte in each compartment. Both compartments are magnetically stirred at 400rpm to ensure homogeneity. The electrolytes used in the anode compartment are either 1M $Ca(ClO_4)_2$ or 1M $NaClO_4$ (depending on the reaction step studied, see next paragraph) from VWR prepared with ultra-pure water (electrical resistivity: 18.2MΩ/cm). In the cathodic compartment, 1M $NaClO_4$ is used for all experiments performed. Calcium carbonate inserted at the anode has a purity ≥99.0% (BioXtra, Sigma-Aldrich). Foils with dimensions 65x25x2mm (total surface area: 36.1cm^2) are used as electrodes. The cathode is made of pure nickel (≥99.5%, Alfa Aesar). At the anode, a dimensionally stable anode (DSA) coated on both sides with mixed metal oxide (12 g/m^2 Ir, Metakem) is used. A cation exchange membrane, Nafion N115 (127 µm thickness, Ion Power GmbH), serves as the separator between the compartments.

The potentiostat and the pH electrode with double-junction are supplied by Metrohm (AutoLab PGSTAT302N & Profitrode). In-situ sampling in each compartment is carried out during the experiments. ICP-AES analyses are performed on the collected samples to measure the calcium ion concentration. XRD analysis was performed on collected precipitates with a Bruker D8 Advanced device with LYNXEYE detectors and a cobalt source. All experiments were performed at room temperature. Experiments at four different currents have been performed: 1.5A (0.042A/cm^2), 1A (0.028A/cm^2), 0.6A (0.017A/cm^2) and 0.3A (0.008A/cm^2). These values have been chosen according to the maximum power of the potentiostat. Due to the large distance between electrodes (15cm), this setup shows low energetic performance (initial cell voltage between 5.3-14.8V depending on the current applied).

For neutral electrolysis experiments, 1M $NaClO_4$ was used in the anodic compartment. Bubble flowmeters were used to define the volumes produced. Gas production measurements are performed until a production of 75cm^3 is reached for each gas. For dissolution experiments, 1M $NaClO_4$ was used in the anodic compartment to obtain accurate Ca^{2+} measurement. An excess of $CaCO_3$ (2.25 times the dissolved quantity expected by the stoichiometry of reaction 5) is inserted at the beginning of the experiment in the anodic compartment. The amount of dissolved calcium is computed by summing the amount of Ca^{2+} found in solution at the anodic and cathodic compartments. The cathodic compartment has been acidified to avoid precipitation that implies a loss of calcium ions in the solution. For migration experiments, 1M $Ca(ClO_4)_2$ was used in the anodic compartment. The cathodic compartment was also acidified for the same reason as the dissolution experiments. For precipitation experiments, only 1M $Ca(ClO_4)_2$ was used in the anodic compartment to maximize Ca^{2+} migration and therefore precipitation. For batch addition experiments of $CaCO_3$, 1M $Ca(ClO_4)_2$ was used in the anodic compartment as well.

Results & Discussion

Neutral water electrolysis

The Faraday efficiencies of the OER and HER have been studied at different applied currents. In accordance with Ellis *et al.* [16], the use of neutral salts such as $NaNO_3$ and $NaClO_4$ was considered first for the electrolytes. However, contrary to Ellis, cost-effective electrode materials rather than platinum were used to ensure industrial feasibility [22]. The choice of electrode materials was guided by the similarity of the hybrid electrolyzer to the chlor-alkali

process (acidic conditions in the anode compartment and alkaline conditions in the cathode compartment) [23, 24]. Consequently, at the anode, a dimensionally stable anode (DSA) coated with IrO_2 was tested and presented an ideal oxygen production rate for both electrolytes. At the cathode, gas measurements with $NaNO_3$ and a pure nickel cathode revealed no discernable hydrogen generation. This phenomenon can be attributed to the preferential reduction of nitrate instead of water, characterized by the following reaction [25]:

$$NO_3^- + H_2O + 2e^- \rightarrow NO_2^- + 2OH^- \quad (7)$$

As a result, the established configuration for the neutral water electrolyzer involves a 1M $NaClO_4$ electrolyte with DSA and nickel. Figures 3A and 3B show the temporal evolution of gaseous H_2 and O_2, respectively, under these conditions at different applied currents and up to 75cm^3 production. The gaseous volumes produced can be re-expressed as a function of supplied charge as illustrated in Figure 3C. The measured slopes for hydrogen and oxygen evolution are 5.4 ± 0.2 and $2.7 \pm 0.1 \cdot 10^{-6}$ mol/C, respectively.

The relation between the applied charge and the amount of gas produced is known as Faraday's law:

$$\frac{dn_{H_2}}{dq} = \frac{1}{2}\frac{dn_{OH^-}}{dq} = \frac{\varepsilon_{F,H_2}}{2F} = \varepsilon_{F,H_2} \cdot 5.2 \cdot 10^{-6} \left[\frac{\text{mol}}{\text{C}}\right] \quad (8a)$$

$$\frac{dn_{O_2}}{dq} = \frac{1}{4}\frac{dn_{H^+}}{dq} = \frac{\varepsilon_{F,O_2}}{4F} = \varepsilon_{F,O_2} \cdot 2.6 \cdot 10^{-6} \left[\frac{\text{mol}}{\text{C}}\right] \quad (8b)$$

with ε_F, F and q the faradaic efficiency, Faraday's constant (96485 C/mol) and the applied charge, respectively.

As can be seen in Fig. 2C, linear regressions over the experimental data yielded estimated slopes that align with the postulated slopes in the Faraday's law for perfect faradic efficiency, i.e. 5.2 and $2.6 \cdot 10^{-6}$ mol/C for H_2 and O_2, respectively. Thanks to equations 8a and 8b, this allows us to calculate the faradic yield, which is equal to 1.04 for both gases. Moreover, the factor 2 difference between both gases also confirms the reaction stoichiometry for electrochemical water splitting (cfr. eq. (3) and (4)). This confirms that the hybrid electrolyzer demonstrates perfect faradic efficiencies across the tested range of current for both H_2 and O_2 production.

Knowing the faradic efficiencies of the OER and HER, the experimental pH in the anodic and cathodic compartments can then be compared to the expected pH, as presented in Figure 4.

Without $CaCO_3$, the pH in the anodic chamber decreases over time due to the oxygen evolution reaction which produces H^+ (see eq. 3). The proton concentration increases in the anodic chamber and is only limited by its migration towards the cathodic chamber, where it will recombine with OH^- to reform water. The expected pH has been computed and fits well with the experimental values, as can be seen in Figure 4. In the anodic compartment, this pH evolution is expressed by equation 9 as a function of the difference between the proton production and migration rate. The transport of ions through the cell comes from three contributions: migration, diffusion and convection. It can be shown that the largest contribution to the total transport through the membrane is migration due to the high current supplied to the cell and that diffusion and convection can be neglected [26, 27].

$$\frac{dpH_{anode}}{dt} = -\log_{10}\left(1 + \frac{1}{[H^+]} * \frac{d[H^+]}{dt}\right) \quad (9a)$$

with :

$$\frac{d[H^+]}{dt} = J_{prod} - J_{migr} = \varepsilon_F \frac{I}{FV} - \frac{I_{H^+}}{FV} \quad (9b)$$

I and I_{H^+} are respectively the total current and the current transported by the migration of H^+, and V is the anodic chamber's volume.

By introducing the transport number, i.e. the fraction of current carried by an ionic species i [28], the previous expression can be re-written and adjusted for the cathodic compartment:

$$\text{Transport number} \equiv t_i = \frac{I_i}{I} = \frac{z_i \mu_i [i]}{\sum_k z_k \mu_k [k]} \quad (10)$$

$$\frac{d[H^+]_{anode}}{dt} = \left(\varepsilon_{F,O_2} - t_{H^+}\right)\frac{I}{FV} \quad (11a)$$

$$\frac{d[H^+]_{cathode}}{dt} = \left(\varepsilon_{F,H_2} - t_{H^+}\right)\frac{I}{FV} \quad (11b)$$

where z_k, μ_k and $[k]$ are the charge number, mobility and concentration of an ionic species k, respectively. From this expression, it appears that an equilibrium pH can be reached when the transport number of H^+ approaches the hydrogen faradaic efficiency, i.e. when the proton migration rate becomes equal to its production rate.

Calcium carbonate dissolution

The calcium carbonate chemical dissolution reaction (5) implies protons and calcium ions as the main reactant and product, respectively. Hence, the study of this step can be done by pH and Ca^{2+} concentration measurements during electrolysis. Figures 5A and 5C illustrate the evolution of the mass of dissolved calcium as a function of time and charge consumed, respectively, while Figures 6A and 6B depict the corresponding pH evolution in the anodic compartment. The amount of calcium dissolved is linearly increasing over time and applied charge. For the latter, a linear regression over all the experimental data gives an estimated slope of $5.2 \pm 0.1 \cdot 10^{-6}$ mol/C. The amount expected if the reaction stoichiometry is followed can be computed from equation 12:

$$\frac{dn_{CaCO_3}}{dq} = -\frac{dn_{Ca^{2+}}}{dq} = -\frac{\varepsilon_D}{2F} = -\varepsilon_D \cdot 5.2 \cdot 10^{-6} \left[\frac{\text{mol}}{\text{C}}\right] \quad (12)$$

with ε_D the chemical dissolution efficiency. Therefore, in view of the fitted slope value, ε_D = 1 regardless of the current applied, and the measured amount of dissolved calcium corresponds to the reaction stoichiometry. This perfect alignment between the experimental and expected slopes demonstrates that the quantity of dissolved calcium is directly linked to the quantity of charge supplied to the hybrid electrolyzer. In other words, the $CaCO_3$ dissolution rate is only limited by the H^+ supply by water electrolysis. An increase in current therefore also increases this dissolution rate. However, a limit could appear if the reaction becomes limited by mass transport. Other parameters that affect the dissolution rate are current, granulometry, agitation (or flowrate in the case of forced flow), solid-liquid fraction and temperature [29].

When an excess of $CaCO_3$ is inserted in the anodic chamber at the beginning of the experiment, Figures 6A and B show that its dissolution consumes the H^+ produced, which implies higher pH values than the ones presented in Fig. 3 and predicted by eq. (11). A pH plateau appears between pH = 6-7 for an applied charge higher than 5kC. This can be explained by resolving equation 13. Indeed, as compared to the previous equation 11a which describes the pH evolution in the anodic compartment without $CaCO_3$, this equation now has an additional term, namely the dissolution efficiency ε_D to take into account the proton consumption during $CaCO_3$ dissolution:

$$\frac{d[H^+]_{anode}}{dt} = \left(\varepsilon_{F,O_2} - t_{H^+} - \varepsilon_D\right)\frac{I}{FV} \quad (13)$$

It has been shown previously that the faradic and dissolution efficiencies $\varepsilon_{F,O2}$ and ε_D were close to one, so these two terms cancel each other out. Moreover, since the proton ionic transport number t_{H+} for a pH value between 6 and 7 is lower than $9 \cdot 10^{-6}$, the pH variation over time tends to zero. At this point, the system can be considered stable and each mole of H^+ produced will be used to dissolve 0.5 mole of $CaCO_3$, also proving that the dissolution reaction is following a perfect stoichiometry. The value of the pH plateau obtained depends on the carbonate equilibrium [30] and could be modified by the same parameters that affect the dissolution rate already mentioned above.

Ca^{2+} migration

The migration efficiency is defined as the ratio between the flux of ions that is effectively migrating across the cationic membrane and the flux expected by the stoichiometry. The expected flux is defined by the global reaction equation (6), where for 4 electrons supplied to the cell, two calcium ions need to migrate and produce two molecules of calcium hydroxide. In other terms, the entire current flowing through the cell must be conducted by these calcium ions to respect the stoichiometry. The transport number of calcium should therefore approach one. The CEM of the hybrid electrolyzer is assumed to block the migration of anions [31]. Therefore, with 1M $NaClO_4$, the transport number equation is solved for sodium, calcium and hydrogen cations. In this case, a large part of the current is transported by the migration of Na^+, lowering the calcium migration efficiency. Indeed, as shown in Figure 7A, the Ca^{2+} transport number could only reach a maximum value of 70% with the sodium-based electrolyte. The utilization of calcium-based electrolytes such as $Ca(ClO_4)_2$ in the anodic chamber has therefore been assessed. With this kind of electrolyte, the migration efficiency only depends on the Ca^{2+} and H^+ concentrations [28]:

$$\varepsilon_M = t_{Ca^{2+}} = \frac{I_{Ca2+}}{I} = \frac{z_{Ca^{2+}}\mu_{Ca^{2+}}[Ca^{2+}]}{(z_{Ca^{2+}}\mu_{Ca^{2+}}[Ca^{2+}]) + (z_{H^+}\mu_{H^+}[H^+])} \quad (14)$$

As a result, a larger fraction of the current is transported by calcium migration, greatly improving its migration efficiency, as illustrated in Figure 7B. In particular, in 1M $Ca(ClO_4)_2$,

the Ca^{2+} transport number remains above 99.9% for pH values above 3.5, and above 99% for values above 2.5. Indeed, at constant Ca^{2+} concentration, the calcium migration efficiency which is directly proportional to the calcium transport number, becomes a function of the pH in the anodic chamber. The same reasoning can be applied to the need to use a cationic membrane instead of a non-selective one. In the latter case, the non-selective membrane will allow the anions to drive the current through the membrane, reducing the calcium ionic transport number.

The mass of Ca^{2+} that migrates has been determined for the different applied currents studied by ICP analysis of samples collected at the cathode. It is shown as a function of time and applied charge in Figure 8A and 8C, respectively. For the latter, the slope of a linear regression is $5.0 \pm 0.1 \cdot 10^{-6}$ mol/C, while the expected slope can be calculated as:

$$\frac{dn_{Ca^{2+}_{mig}}}{dq} = \frac{\varepsilon_M}{2F} = \varepsilon_M \cdot 5.2 \cdot 10^{-6} \left[\frac{mol}{C}\right] \quad (15)$$

Therefore, the experimental migration efficiency ε_M is again nearly 100%. This value can be explained by a pH value close to neutrality and the use of a calcium-based electrolyte. As mentioned previously, with an excess of calcium carbonate, the anodic pH stabilizes at high values above pH=6. With 1M $Ca(ClO_4)_2$ electrolyte, this implies a Ca^{2+} transport number very close to one. The amount of Ca^{2+} that migrates is then proportional to the amount of charge provided and identical to the amount of Ca^{2+} that is dissolved.
The evolution of the amount of Ca^{2+} in the anodic chamber can now be determined thanks to the dissolution and migration rate:

$$\frac{dn_{Ca^{2+}_{anode}}}{dq} = (\varepsilon_D - \varepsilon_M)\frac{1}{2F} \left[\frac{mol}{C}\right] \quad (16)$$

In the previous sections, it has been demonstrated that the dissolution and migration efficiencies ε_D and ε_M were both close to 100%. As a result, the dissolution and migration rates are also very similar, which is also confirmed by comparing Figure 5B and Figure 8B, so that the amount of calcium ions in the anodic chamber should remain constant. In other words, the migrating Ca^{2+} ions are constantly renewed by the $CaCO_3$ dissolution.

$Ca(OH)_2$ precipitation

Measurements of Ca^{2+} concentration and pH in the cathodic chamber for an applied current of 0.6A and 1.5A are shown in Figure 9. As expected, the Ca^{2+} concentration in the cathodic chamber is first steadily increasing, driven by its migration. Simultaneously, the pH in the cathodic chamber follows a rise due to the HER producing OH^- groups (cfr. eq. 4). The slope of the calcium ion concentration increase is equal to $5.1 \pm 0.1 \cdot 10^{-6}$ mol/C for 0.6A and $3.8 \pm 0.2 \cdot 10^{-6}$ mol/C for 1.5A. For an applied current of 0.6A, white precipitates of $Ca(OH)_2$ start appearing in the solution after approximately 2h30min of experiment. At the same time, even though Ca^{2+} migration and OH^- production continues, their concentrations stabilize.

The mass of calcium hydroxide precipitated is difficult to obtain experimentally due to its partial deposition on the cathode surface and the membrane. It is therefore more convenient to extract the precipitation efficiency ε_P from the amount of calcium ions in the cathodic compartment:

$$\frac{dn_{Ca^{2+},cathode}}{dq} = (\varepsilon_M - \varepsilon_P)\frac{1}{2F}\left[\frac{mol}{C}\right] \tag{17}$$

Since the number of calcium ions at the cathode is known by ICP analysis and it has been shown before that ε_M is equal to one, the precipitation efficiency ε_P can be computed from this equation. During the initial linear increase in Ca^{2+} concentration, ε_P is equal to about 2% and 26% for 0.6A and 1.5A respectively. Once the plateau is reached, the calcium ion concentration and pH no longer fluctuate. According to eq. (17), this then implies that ε_P becomes close to one, proving that the precipitation follows the reaction stoichiometry.

The precipitation of $Ca(OH)_2$ starts once the activities of Ca^{2+} and OH^- ($a_{Ca^{2+}}$ and a_{OH^-}) are sufficiently high for the solubility limit K_s of $Ca(OH)_2$ to be exceeded [32, 33]:

$$K_s = a_{Ca^{2+}}a_{OH^-}^2 = (\gamma_{Ca^{2+}}[Ca^{2+}])(\gamma_{OH^-}[OH^-])^2 = 5.02 \cdot 10^{-6} \tag{18}$$

The activity of a species is defined as the product of an activity coefficient, which itself depends on the ionic strength of the electrolyte solution, and the species concentration. The activity coefficients can be calculated with the Davies equation [34] and have a value between 0.40-0.43 and 0.79-0.81 for Ca^{2+} and OH^- respectively for the range of concentrations observed in the cathodic compartment.

In Figure 9, the measured cathodic pH is compared for each Ca^{2+} concentration to the minimum pH needed to allow precipitation of $Ca(OH)_2$ This theoretical pH represents the OH^- concentration needed to exceed the solubility limit described in equation (18). The comparison indicates that precipitation starts as soon as the measured pH in the cathodic chamber reaches this theoretical value, as indicated by the vertical dashed lines both at 0.6 A (left) and 1.5 A (right). Indeed, from that point onwards, both the measured pH and Ca^{2+} concentration stabilize at the plateau value predicted by the solubility product. An alternative presentation of the evolution of the Ca^{2+} and OH^- activities towards precipitation is given for both applied currents in Figure 10. It can be seen that the two experiments are not reaching the same equilibrium state. Moreover, the time evolution at 1.5 A deviates from the expected behavior. This can be taken as indicative for the occurrence of preliminary precipitation at the surface of the cathode and/or the membrane, resulting from the presence of a pH gradient within the cathode compartment. Indeed, the generation of OH^- at the cathode leads to the appearance of a higher local pH, implying early heterogeneous precipitation on any neighboring solid surface.

Results from XRD analysis on the precipitates retrieved from, respectively, the cathode, the bulk solution and on the membrane are shown in Figure 11. The perfect fit with the theoretical $Ca(OH)_2$ portlandite peaks proves that the white precipitates formed are made of nearly pure portlandite. A small amount of sodium coming from the electrolyte was detected in the precipitate by ICP analysis (1.4wt.%).For both precipitates, a specific surface area and pore volume of, respectively, 0.6 m^2/g and 0.002 cm^3/g has been determined by BET analysis. A particle size distribution (PSD) analysis showed that all precipitates had a characteristic size below 70 µm. These values are comparable to previously published values of 0.8 m^2/g and 90 µm [16]. The hydrated lime produced by our hybrid electrolyzer can therefore be used directly for construction and civil engineering applications [35]. However, its specific surface area and porous volume are too low for environmental applications such as flue gas cleaning, the latter typically requiring 10~40 m^2/g and 0.2 cm^3/g [36].

Process upscaling

In the previous section, it was already pointed out that although $Ca(OH)_2$ precipitation followed the expected reaction stoichiometry from eq. (6), its preferential location on the cathode and membrane surface can still be problematic for the large-scale viability of the process. Therefore,

in order to analyze a potential change in the preferential location of precipitation, continuous additions of small $CaCO_3$ quantities were compared to the one-step batch addition of $CaCO_3$ at the beginning of the experiment. Pictures of the different membranes after 6h experiments are shown in Figure 12. $Ca(OH)_2$ is clearly seen to precipitate in different zones of the cathodic chamber depending on the operating scenario. In the case without $CaCO_3$ addition (Fig. 11A), Ca^{2+} ions can only come from the $Ca(ClO_4)_2$ electrolyte in the anodic chamber, and precipitation mainly occurs in solution and on the surface of the cathode rather than on the membrane. When an excess of $CaCO_3$ is added at the beginning, precipitates mainly localize on the cathodic side of the CEM, as illustrated in Figure 12B. In that case, precipitation completely obstructs the membrane, dropping drastically the CEM's performance (40.1% of cell voltage increase for the experiment at 1.5A) by hindering the passage of any ionic species. For longer experiments (~24h), the membrane even starts fracturing causing the two compartments to partially mix together.

All this indicates that, despite agitation in the cell, the pH profile across the cathodic chamber is not constant. Precipitation will be initiated as soon as the required pH is reached. The first location in the migration path of Ca^{2+} that presents this pH will thus be subject to precipitation. To anticipate this location, 2 phenomena must be considered. On the one hand OH^- production at the cathode and its migration towards the CEM, where it is being accumulated due to concentration polarization effects [27, 37]. On the other hand the migration of H^+ through the CEM and its combination with OH^- in the cathodic compartment to reform water. In the absence of $CaCO_3$, no H^+ are being consumed so that the pH in the anodic compartment reaches low values, as already indicated in Figure 4 and shown again in Figure 13A. According to Figure 7B, this then implies a decrease of the Ca^{2+} transport number, in favor of an increase in the H^+ transport number. This favored migration of H^+ and its recombination with OH^- is lowering the pH at the cathodic side of the membrane thus limiting the risk of precipitation. In this case, the required pH will first be reached at the cathode surface where OH^- are being generated. This explains the preferential localization of precipitation on the cathode's surface. As can been seen on Figure 13B, the advantage of the absence of any precipitation on the membrane is counterbalanced by a decrease of the migration efficiency with time due to a decrease of the pH.

Conversely, with an excess of $CaCO_3$ being added at the beginning, the Ca^{2+} migration efficiency remains at almost 100%, minimizing the migration of H^+ and its recombination with OH^-. The migrating OH^-, blocked by the CEM, therefore accumulate in its vicinity, leading to a significant increase in pH close to the cathodic side of the membrane. Consequently, the

migrating Ca^{2+} encounter this high OH^- concentration and precipitates on the membrane itself. This is in line with previous observations showing that the migration of H^+ and its impact on the pH gradient inside the cathodic compartment plays an important role in the precipitation localization [38, 39].

Finally, Figure 13B also illustrates the impact of repetitive batch additions of $CaCO_3$ on the precipitation occurring on the CEM. By carefully selecting an appropriate working pH range, which also allows to ensure that the anodic compartment remains in the CO_2 stability region, it becomes possible to regulate the Ca^{2+} migration efficiency. This then allows to find a compromise between Ca^{2+} and H^+ migration. For instance, with such batch additions, the pH can be kept between 1.5 and 2 (Figure 13A), so that the Ca^{2+} migration efficiency on Figure 13B remains still sufficiently high around 92~97%. At the same time, more H^+ are allowed to migrate and recombine with OH^-, thus reducing the likelihood of $Ca(OH)_2$ precipitation on the CEM.

Conclusions

A novel method for the electrochemical decarbonation of $CaCO_3$ into $Ca(OH)_2$ has been successfully demonstrated in a specific two-compartment electrochemical cell and validated at different applied currents. Compared to the three-compartment configuration commonly used, this configuration has the advantage of simplifying the design, minimizing the inter-electrode distance and only requiring one (cationic) membrane. First of all, the stoichiometric production of both H_2 and O_2 gas in a neutral electrolyte has been verified, exhibiting perfect faradaic efficiencies using and hence cost-effective platinum-free electrodes. Moreover, the establishment of a pH gradient between the anodic and cathodic compartment was confirmed, as well as its charge dependency. In the anodic chamber, the acidic pH generated by the OER allows for the stoichiometric dissolution of $CaCO_3$, only being limited by the supply of H^+, which in turn is directly linked to the applied current. The resulting calcium ions were then shown to migrate towards the cathode with a migration efficiency depending on its transport number. The use of a CEM to separate both chambers and a calcium-based electrolyte (e.g. 1M $Ca(ClO_4)_2$) are essential to ensure a near-perfect Ca^{2+} migration efficiency, hence avoiding current transport by species other than calcium ions. In the cathodic chamber, the HER generates an alkaline pH enabling the precipitation of pure $Ca(OH)_2$ with near-ideal

stoichiometry. The precipitation equilibrium can be predicted provided that the activity coefficients of the different ionic species are taken into account.

Moreover, by systematically studying the current dependency of each of the above steps, the experimentally observed time and charge dependency of both Ca^{2+} and OH^- ions was shown to follow a near-perfect reaction stoichiometry. Constitutive rate equations could therefore be presented that allow to predict the temporal variation of pH and calcium ion concentration in both the anodic and cathodic chambers, including their current dependencies. Finally, with respect to a possible upscaling of the process, practical issues related to the risk of $Ca(OH)_2$ precipitation onto the CEM and onto the cathode have been addressed. To mitigate this, controlled multiple batch additions of $CaCO_3$ as opposed to a one-time excess addition were demonstrated to allow to regulate the precipitation behavior by controlling the working pH in the anodic compartment. This in turn allows to tune the balance between Ca^{2+} and H^+ migration, resulting in a minimization of local pH gradients in the cathodic chamber and therefore also the risk of precipitation onto the CEM.

Acknowledgements

This work was supported by the Belgian Regional Walloon project Faraday (grant number 8512).

References

[1] European Lime Association, "A pathway to negative CO2 emissions by 2050," 2023.

[2] A. Dowling, J. O'Dwyer and C. C. Adley, "Lime in the Limelight," *Journal of Cleaner Production,* vol. 92, pp. 13-22, 2015.

[3] L. Bing, M. Ma, L. Liu, J. Wang, L. Niu and F. Xi, "An investigation of the global uptake of CO2 by lime from 1930 to 2020," *Earth System Science Data,* vol. 15, no. 6, p. 2431–2444, 2023.

[4] P. O. George, A. S. Gutiérrez, J. C. Martínez and C. Vandecasteele, "Cleaner production in a small lime factory by means of process control," *Journal of Cleaner Production,* vol. 18, no. 12, pp. 1171-1176, 2010.

[5] T. P. Hillsa, M. Sceatsb, D. Rennieb and P. Fennella, "LEILAC: Low cost CO2 capture for the cement and lime industries," *Energy Procedia,* vol. 114, p. 6166 – 6170, 2017.

[6] M. Simoni, M. D. Wilkes and S. Brown, "Decarbonising the lime industry: State-of-the-art," *Renewable and Sustainable Energy Reviews,* vol. 168, p. 112765, 2022.

[7] A. S. Gutiérreza, J. Van Caneghem, J. B. Cogollos Martínezа and C. Vandecasteele, "Evaluation of the environmental performance of lime production in Cuba," *Journal of Cleaner Production,* vol. 31, pp. 126-136, 2012.

[8] G. Habert, S. Miller, V. John, J. Provis, A. Favier, Horvath, A. and K. Scrivener, "Environmental impacts and decarbonization strategies in the cement and concrete industries," *Nature Reviews Earth & Environment,* vol. 1, pp. 559-573, 2020.

[9] L.-M. Bjerge and P. Brevik, "CO2 Capture in the Cement Industry, Norcem CO2 Capture Project (Norway)," *Energy Procedia,* vol. 63, pp. 6455-6463, 2014.

[10] M. Plaza, S. Martínez and F. Rubiera, "CO2 Capture, Use, and Storage in the Cement Industry : State of the Art and Expectations," *Energies,* vol. 13, no. 21, p. 5692, 2020.

[11] S. Griffithsa, B. K. Sovacoolb, D. D. Furszyfer Del Rioa, A. M. Foleyd, M. D. Bazilianf, J. Kimg and J. M. Uratani, "Decarbonizing the cement and concrete industry: A systematic review of socio-technical systems, technological innovations, and policy options," *Renewable and Sustainable Energy Reviews,* vol. 180, p. 113291, 2023.

[12] K. Goto, S. Kazama, A. Furukawa, M. Serizawa, S. Aramaki and K. Shoji, "Effect of CO2 purity on energy requirement of CO2 capture processes," *Energy Procedia,* vol. 37, pp. 806-812, 2013.

[13] M. Pisciottaa, H. Pilorge, J. Davids and P. Psarras, "Opportunities for cement decarbonization," *Cleaner Engineering and Technology,* vol. 15, p. 100667, 2023.

[14] T. Hanein, M. Simoni, C. L. Woo, J. L. Provis and H. Kinoshita, "Decarbonisation of calcium carbonate at atmospheric temperatures and pressures, with simultaneous CO2 capture, through production of sodium carbonate," *Energy & Environmental Science,* vol. 14, no. 12, pp. 6595-6604, 2021.

[15] S. V. Castano, E. C. LaPlante, S. Shimoda, B. Wang, N. Neithalath, G. Sant and L. Pilon, "Calcination-free production of calcium hydroxide at sub-boiling temperatures," *RSC Advances,* vol. 11, no. 3, pp. 1762-1772, 2021.

[16] L. D. Ellis, A. F. Badel and M. L. Chiang, "Toward electrochemical synthesis of cement—An electrolyzer-based process for decarbonating CaCO3 while producing useful gas streams," *PNAS,* vol. 117, no. 23, pp. 12584-12591, 2019.

[17] Z. Congquan , N. Jihong and C. Huiqi, "Harnessing Electrochemical pH Gradient for Direct Air Capture with Hydrogen and Oxygen By-Products in a Calcium-Based Loop," *Sustainable Energy & Fuels,* vol. 5, no. 17, pp. 4355-4367, 2021.

[18] A. W. M. Benjamin, B. Z. Zishuai, T. E. P. Colin and P. B. Curtis, "Electrochemical Cement Clinker Precursor Production at Low Voltages," *ACS Energy Letters,* vol. 8, no. 4, pp. 1772-1778, 2023.

[19] X. Qixian, W. Lili, Z. Zhuang and L. Jingshan, "Electrochemical transformation of limestone into calcium hydroxide and valuable carbonaceous products for decarbonizing cement production," *iScience,* vol. 26, no. 2, p. 106015, 2023.

[20] Z. Zhang, B. A. Mowbray, C. T. Parkyn, C. Waizenegger, A. S. Williams, E. W. Lees, S. Ren, Y. Kim, R. P. Jansonius and C. P. Berlinguette, "Cement clinker precursor production in an electrolyser," *Energy & Environmental Science,* vol. 15, no. 12, pp. 5129-5136, 2022.

[21] N. Jihong, Z. Jiayin, B. Jinhong and G. Xiaofei, "Recycling the cathode materials of spent Li-ion batteries in a H-Shaped neutral water electrolysis cell," *Separation and Putification Technology ,* vol. 278, p. 119485, 2022.

[22] D. M. Heard and A. J. Lennox, "Electrode Materials in Modern Organic Electrochemistry," *Angewandte Chemie,* vol. 59, no. 43, pp. 18866-18884, 2020.

[23] F. Franco, J. Prior, S. Velizarov and A. Mendes, "A Systematic Performance History Analysis of a Chlor-Alkali Membrane Electrolyser under Industrial Operating Conditions," *Applied Sciences,* vol. 9, no. 2, p. 284, 2019.

[24] K. Li, Q. Fan, H. Chuai, H. Liu, S. Zhang and X. Ma, "Revisiting Chlor-Alkali Electrolyzers: from Materials to Devices," *Transactions of Tianjin University,* vol. 27, pp. 202-216, 2021.

[25] K. Kim, S.-H. Paik and C. K. Rhee, "Water Electrolysis Accompanied by Side Reactions," *Journal of Chemical Education,* vol. 98, p. 2381−2386, 2021.

[26] S. Ozkul, J. Van Daal and N. Kuipers, "Transport mechanisms in electrodialysis: The effect on selective ion transport in multi-ionic solutions," *Journal of Membrane Science,* vol. 665, p. 121114, 2023.

[27] T. Luoa, S. Abdua and M. Wessling, "Selectivity of ion exchange membranes : A review," *Journal of Membrane Science,* vol. 555, pp. 429-454, 2018.

[28] M. R. Wright, An Introduction to Aqueous Electrolyte Solutions, Chichester: John Wiley & Sons , 2007.

[29] C. B. McAuley, M. J. Yang, R. Rickaby and R. C. Compton, "Calcium Carbonate Dissolution from the Laboratory to the Ocean: Kinetics and Mechanism," *Chemistry Europe,* vol. 28, no. 68, pp. 1-11, 2022.

[30] R. Zeebe and D. Wolf-Gladrow, CO2 in Seawater: Equilibrium, Kinetics, Isotopes, Elsevier Science, 2001.

[31] K. Yang and M. Qin, "The Application of Cation Exchange Membranes in Electrochemical Systems for Ammonia Recovery from Wastewater," *Membranes,* vol. 11, no. 7, p. 494, 2021.

[32] V. Snoeyink and D. Jenkins, Water Chemistry, John Wiley & Sons, 1980.

[33] D. W. Green and R. H. Perry, Perry's Chemical Handbook, Eighth Edition, McGraw-Hill, 2008.

[34] E. Samson, G. Lemaire, J. Marchand and J. J. Beaudoin, "Modeling chemical activity effects in strong ionic solutions," *Computational Materials Science,* vol. 15, no. 3, pp. 285-294, 1999.

[35] A. Padovnik and V. B. Bosiljkov, "The Influence of Dry Hydrated Limes on the Fresh and Hardened Properties of Architectural Injection Grout," *Materials,* vol. 14, no. 19, p. 5585, 2021.

[36] D. L. Moran and M. Rostam-Abadi, "High surface area hydrated lime and method of removing SO2 from a gas stream". US Patent 5492685A, 1996.

[37] M. B. S. Ali, A. Mnif and B. Hamrouni, "Modelling of the limiting current density of an electrodialysis process by response surface methodology," *Ionics,* vol. 24, p. 617–628, 2018.

[38] S. Mikhaylin and L. Bazinet, "Fouling on ion-exchange membranes: Classification, characterization and strategies of prevention and control," *Advances in Colloid and Interface Science,* vol. 229, pp. 34-56, 2015.

[39] C. Casademont, M. A. Farias, G. Pourcelly and L. Bazinet, "Impact of electrodialytic parameters on cation migration kinetics and fouling nature of ion-exchange membranes during treatment of solutions with different magnesium/calcium ratios," *Journal of Membrane Science,* vol. 325, no. 2, pp. 570-579, 2008.

Figure legends

Fig. 1. (top) Comparison between the thermal and electrochemical production route of $Ca(OH)_2$; (bottom) a simplified reaction scheme of the hybrid electrolyzer used in this work.

Fig. 2. Schematic representation of the experimental setup

Fig. 3. Evolution of produced volumes of hydrogen (A) and oxygen (B) at different current densities as a function of time and charge (C).

Fig. 4. Experimental (symbols) and theoretical (lines) pH evolution in the anodic and cathodic chamber as a function of time (A) and applied charge (B) in the absence of $CaCO_3$.

Fig. 5. Mass of dissolved Ca^{2+} as a function of (A) time and (C) applied charge ; (B) $CaCO_3$ dissolution rate as a function of applied current, as determined from the slopes in (A).

Fig. 6. Experimental pH evolution in the anodic chamber as a function of time (A) and applied charge (B) when adding an excess of $CaCO_3$ at the beginning. The solid line represents the expected pH evolution in the absence of $CaCO_3$.

Fig. 7. Ca^{2+} transport number as a function of pH and Ca^{2+} concentration in the case of (A) 1M $NaClO_4$ and (B) 1M $Ca(ClO_4)_2$ electrolytes.

Fig. 8. Mass of migrated Ca^{2+} in the cathodic chamber as a function of (A) time and (C) applied charge ; (B) Ca^{2+} migration rate as a function of applied current, as determined from the slopes in (A).

Fig. 9. Temporal evolution in the cathodic chamber of Ca^{2+} concentration (left axis) and pH (right axis) for an applied current of (A) 0.6A and (B) 1.5A.

Fig. 10. Measured (symbols) and expected (line) evolution of Ca^{2+} vs. OH^- activity from the same experiments shown in Fig. 8. The theoretical $Ca(OH)_2$ solubility product is indicated by the red solid line.

Fig. 11. X-ray diffractograms after 6hr at 0.6 A of the precipitates collected on the cathode and membrane surfaces, respectively.

Fig. 12. Optical micrographs of the cationic exchange membrane taken from the cathodic side at the end of three different 6 h longexperiments at 0.6A : (A) without $CaCO_3$ addition ; (B) with an excess of $CaCO_3$ added at the beginning ; (C) with several batch additions of $CaCO_3$ in order to keep the pH between 1.5 and 2.

Fig. 13. (A) pH evolution in the anodic compartment and (B) experimental and theoretical Ca^{2+} migration efficiency as a function of time with an applied current of 0.6A for the same 3 operating scenarios as in Fig. 11.

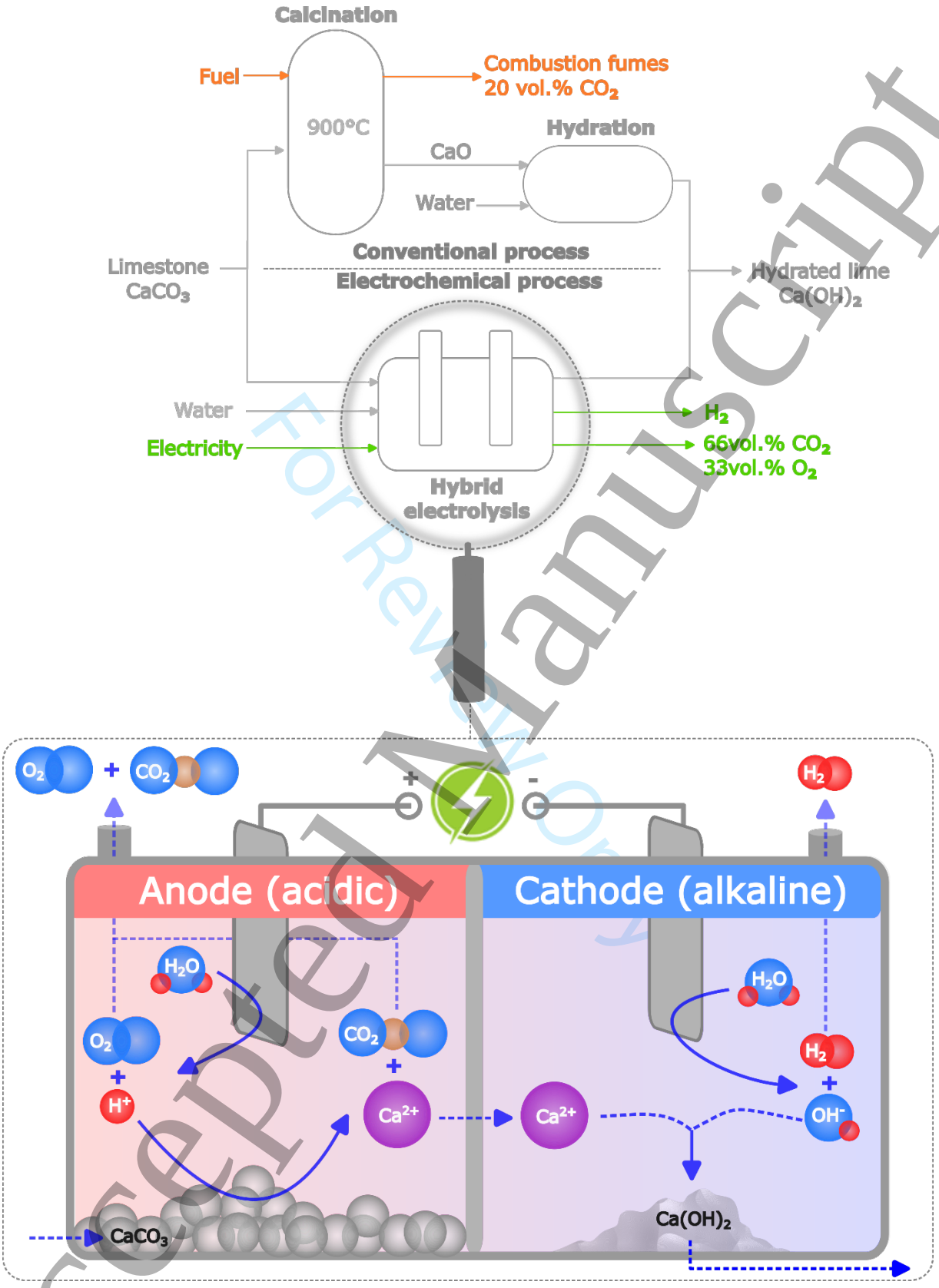

Figure 1

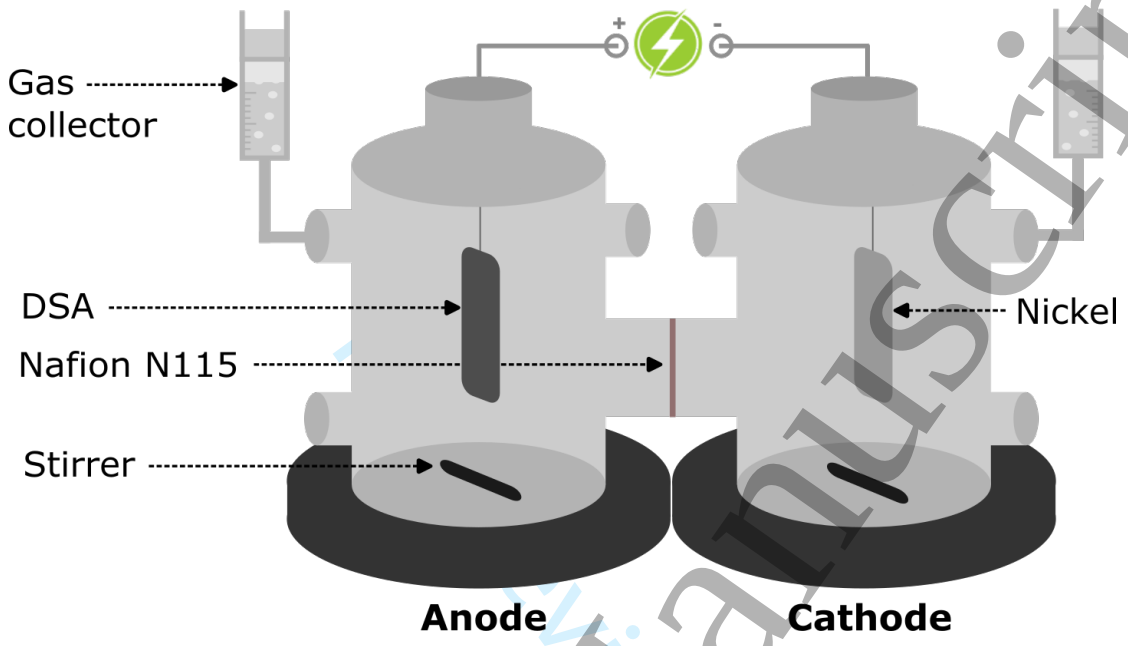

Figure 2

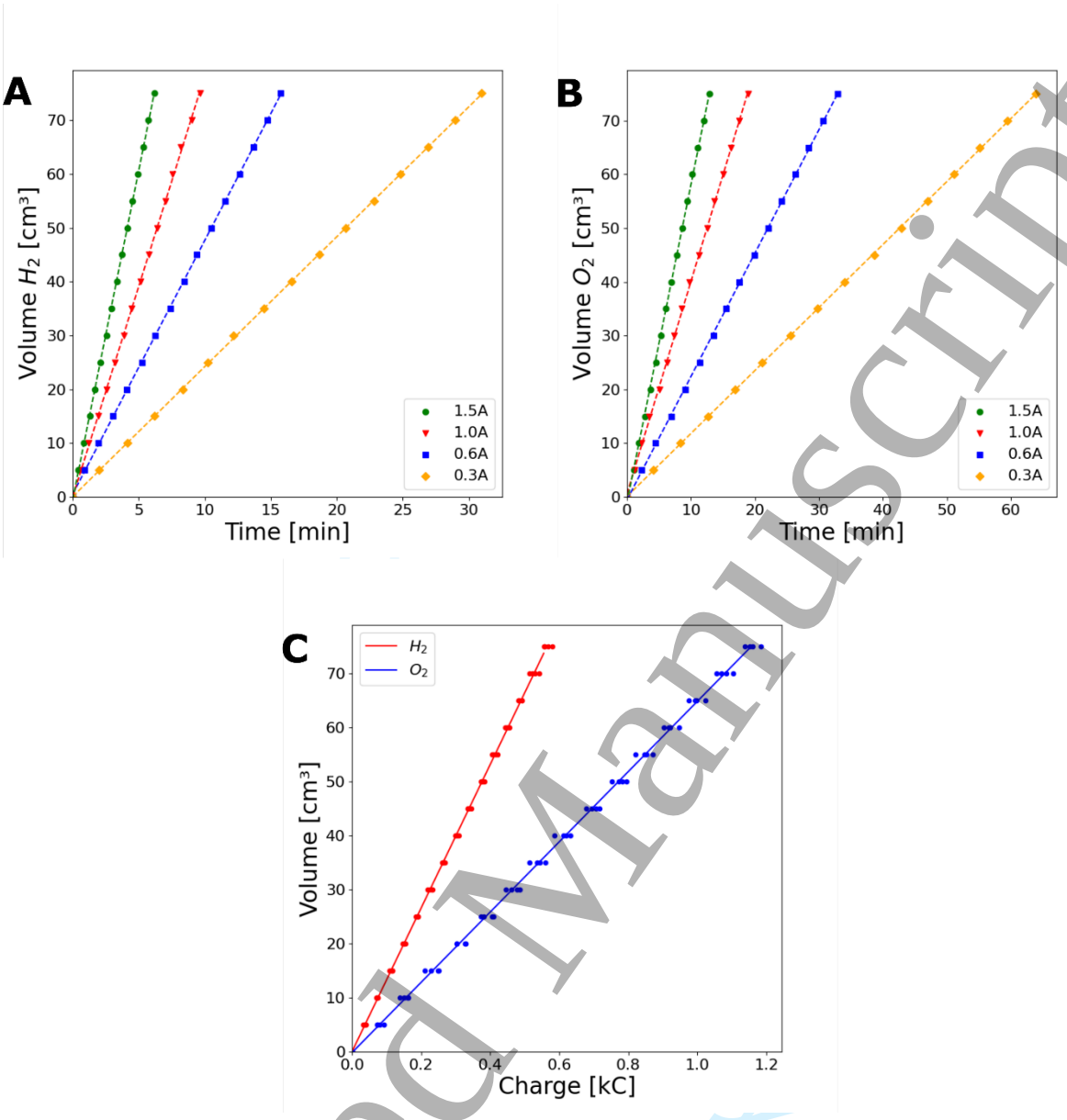

Figure 3

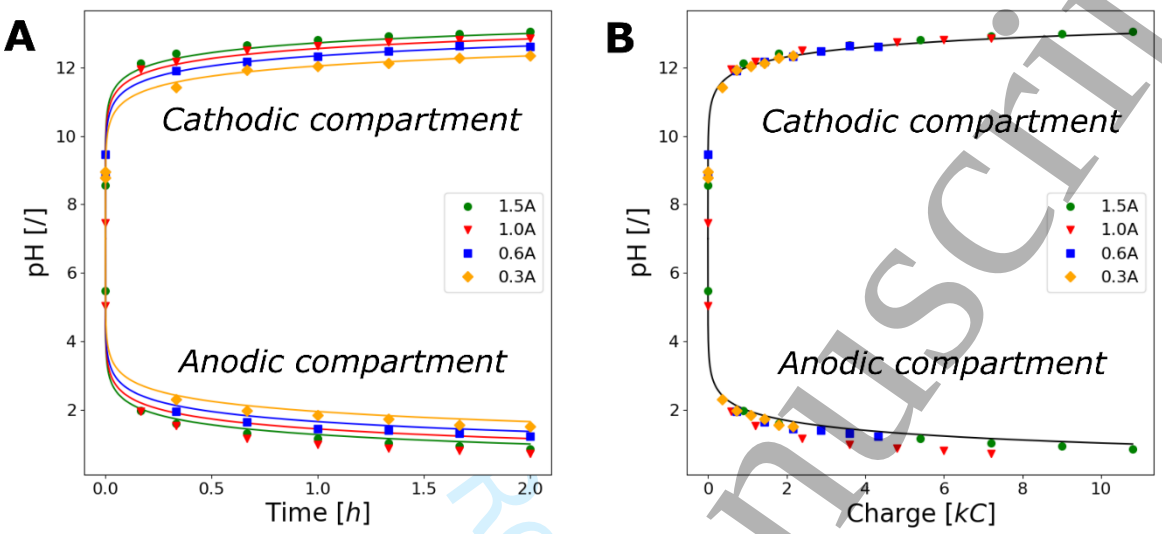

Figure 4

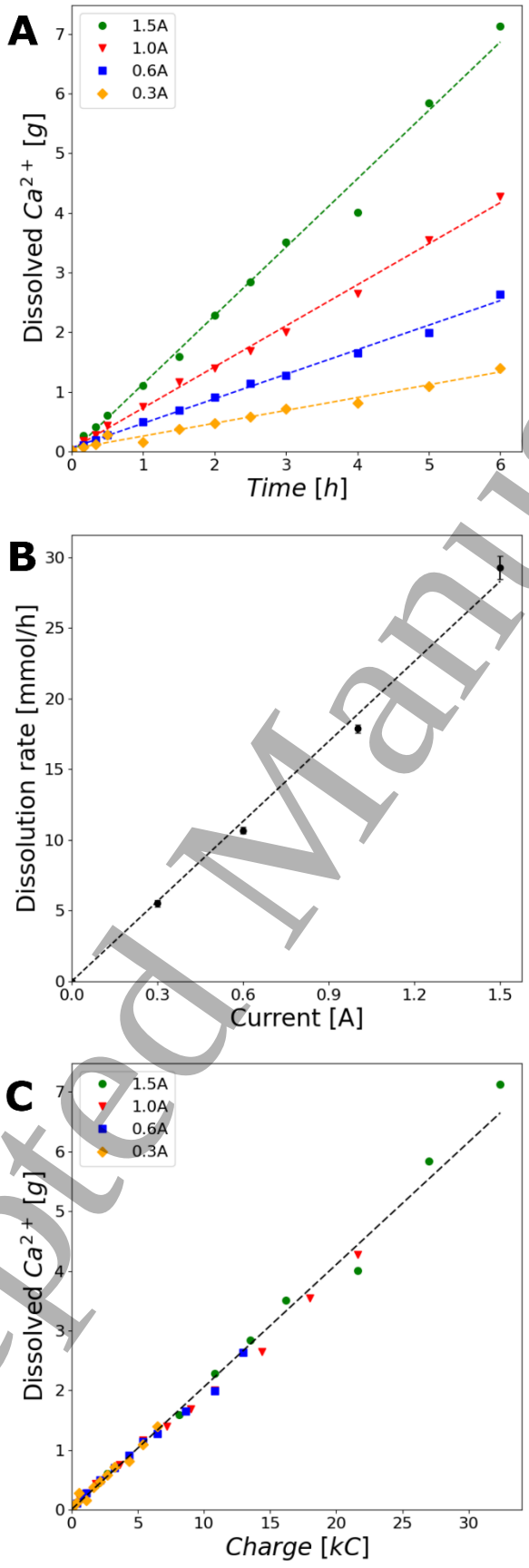

Figure 5

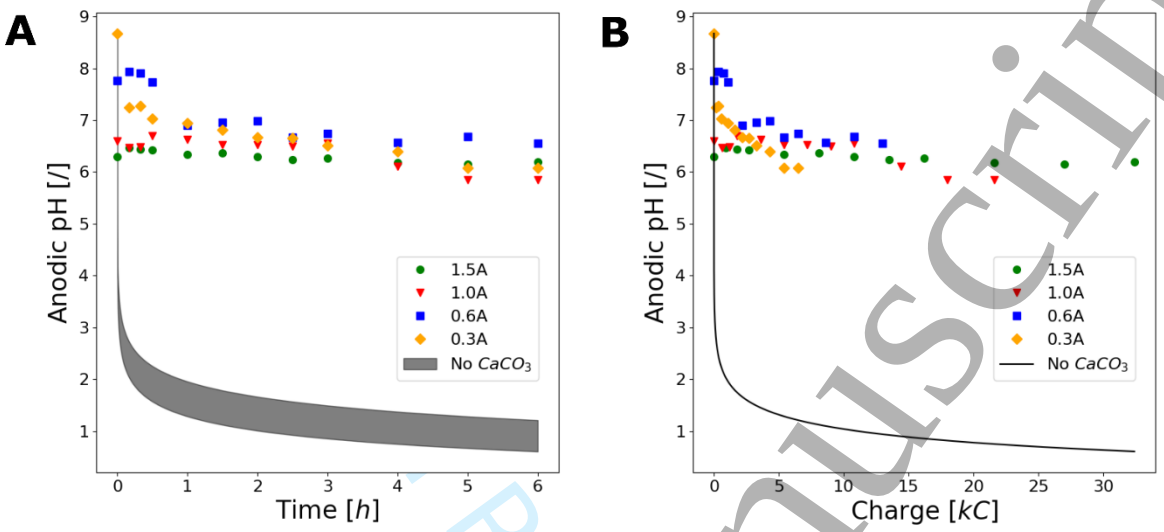

Figure 6

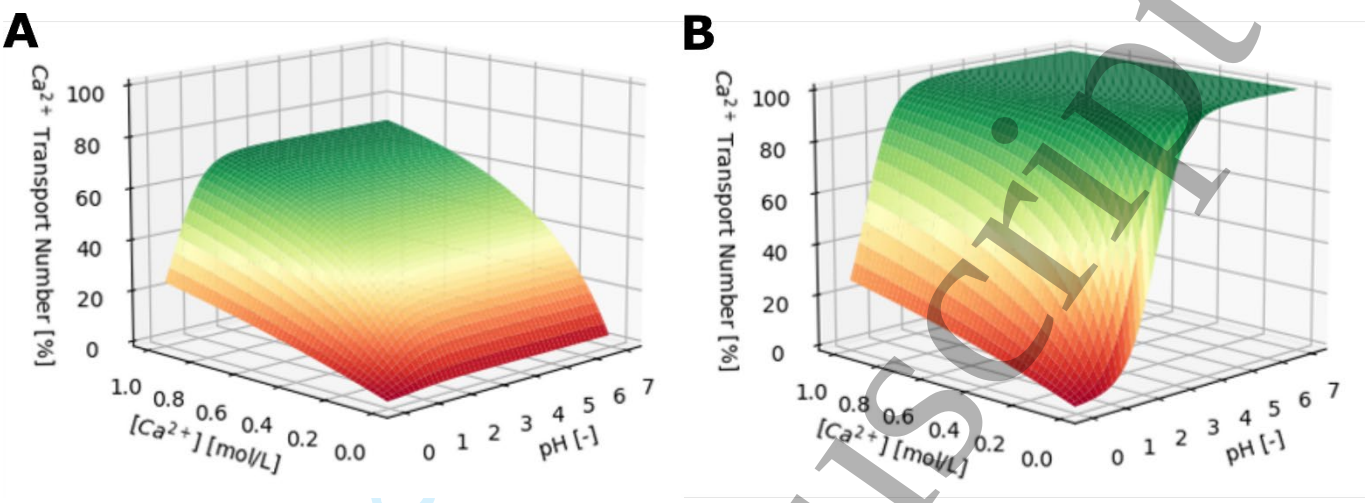

Figure 7

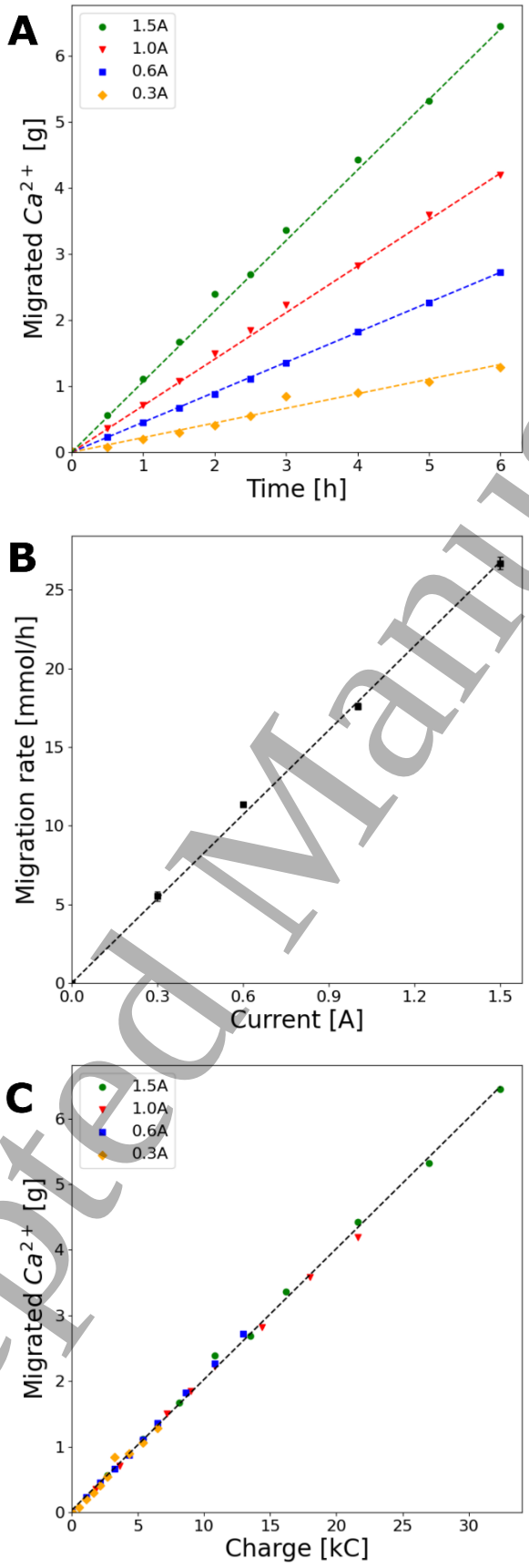

Figure 8

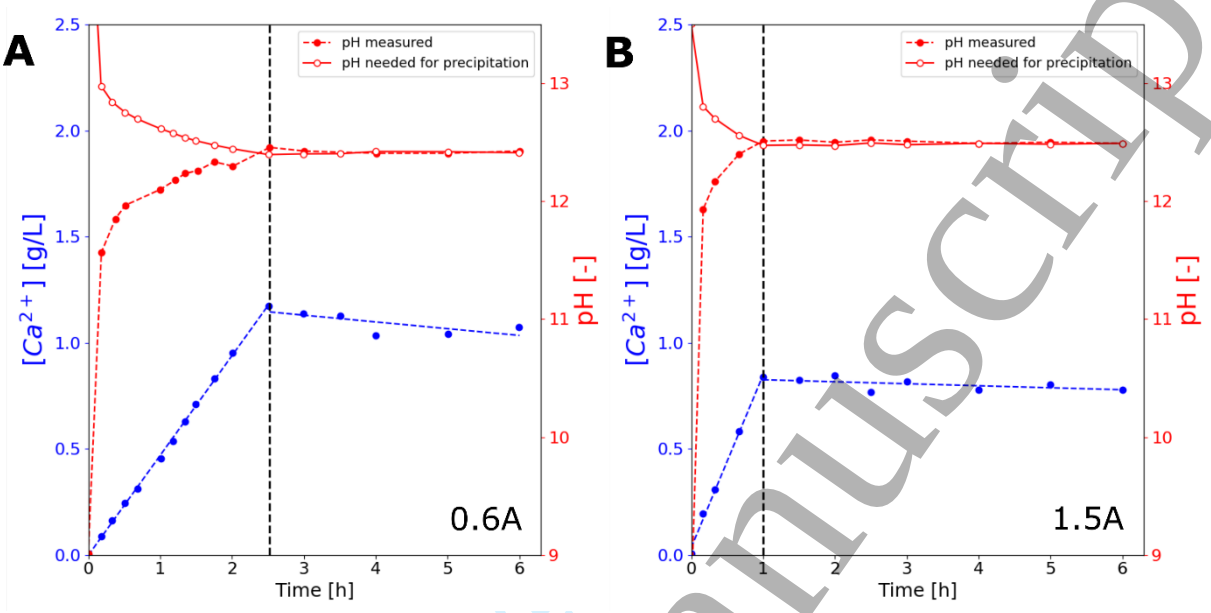

Figure 9

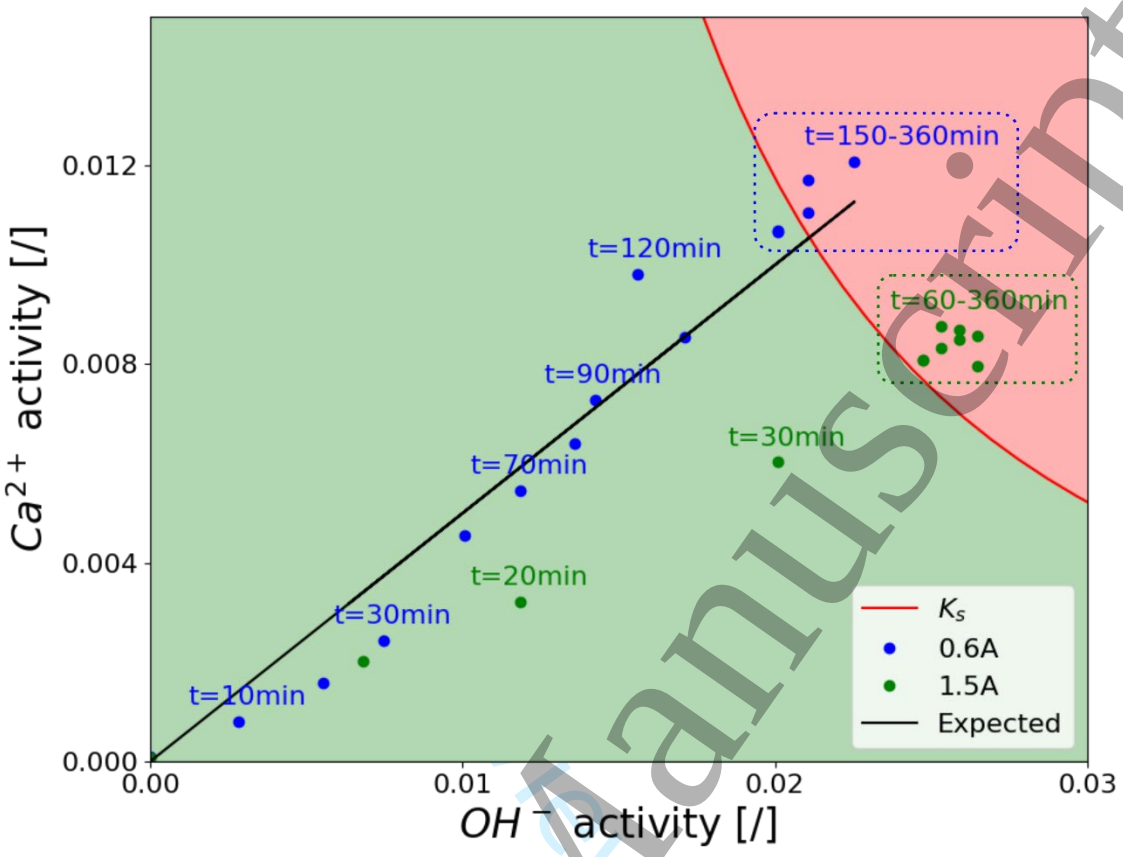

Figure 10

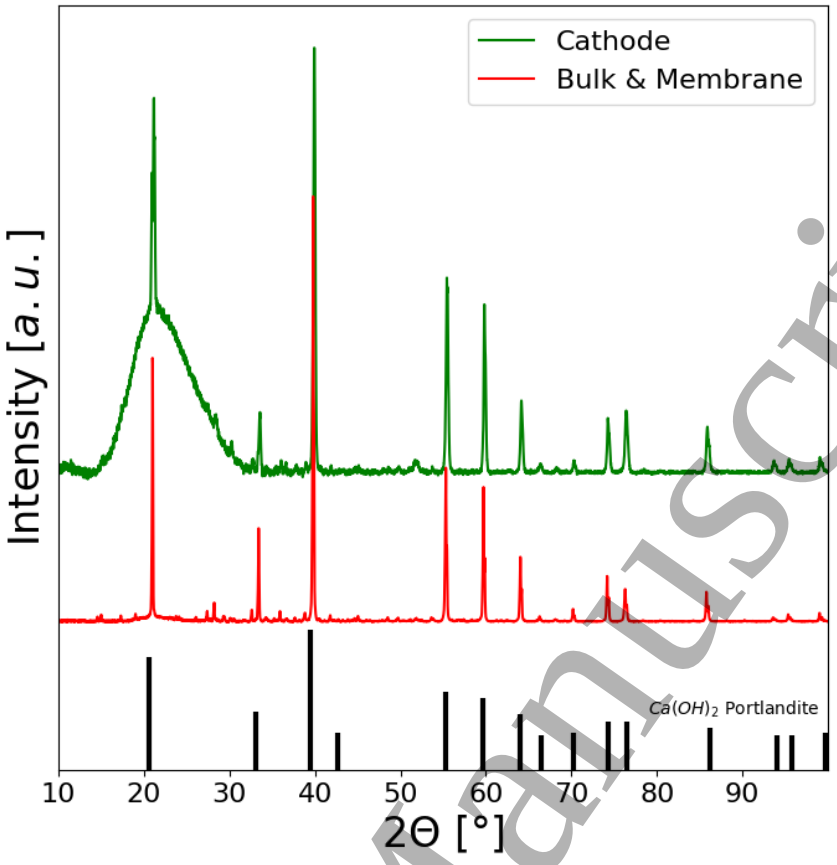

Figure 11

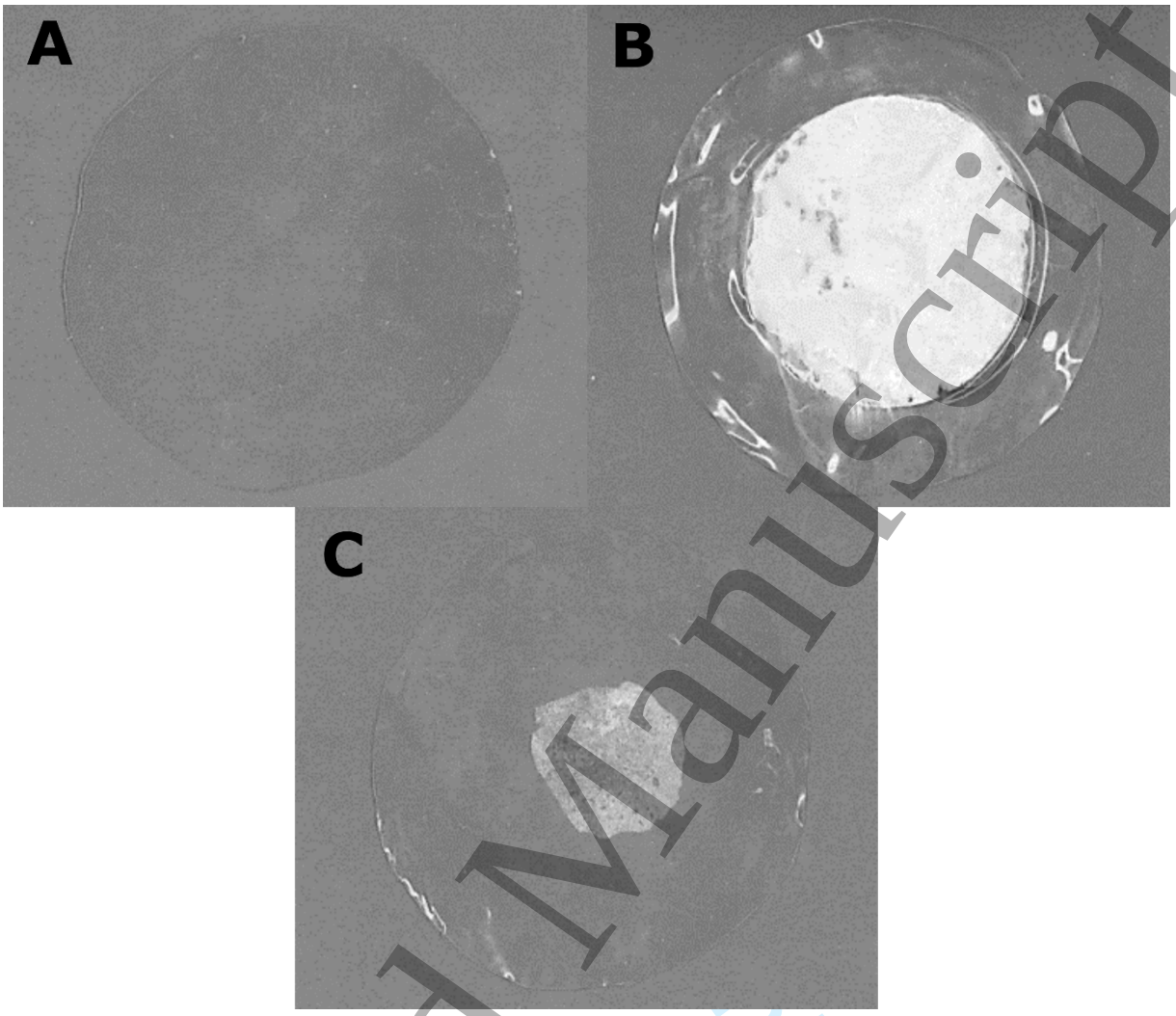

Figure 12

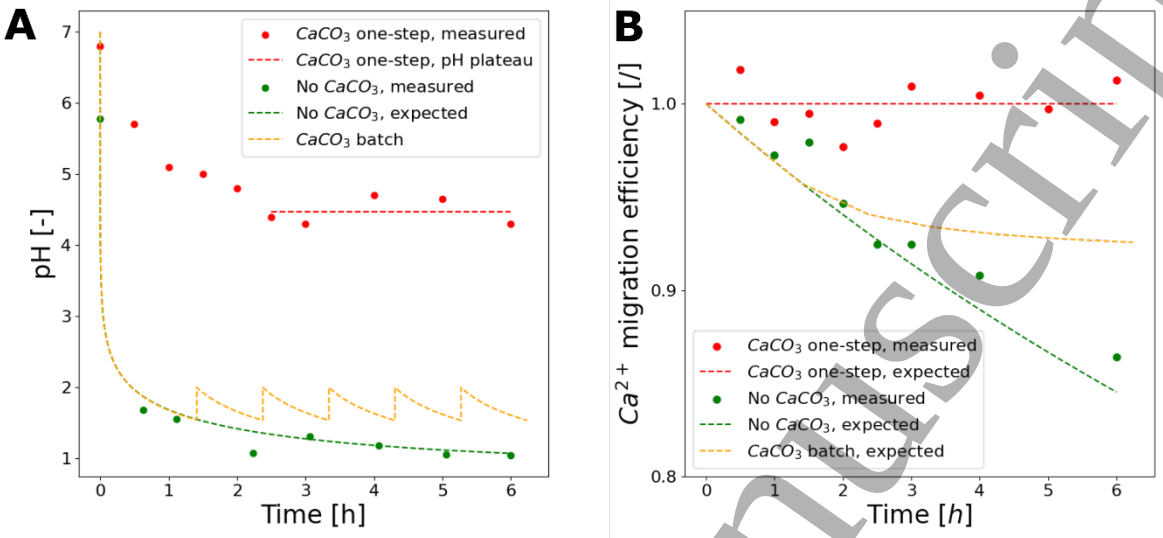

Figure 13